Title

Mineralogical, nanostructural, and Ca isotopic evidence for non-classical calcium phosphate mineralization at circum-neutral pH

Authors

Schilling, Kathrin
Brown, Shaun T
Lammers, Laura N

Publication Date

2018-11-01

DOI

10.1016/j.gca.2018.08.019

Peer reviewed

Available online at www.sciencedirect.com

ScienceDirect

Geochimica et Cosmochimica Acta 241 (2018) 255–271

Geochimica et Cosmochimica Acta

www.elsevier.com/locate/gca

Mineralogical, nanostructural, and Ca isotopic evidence for non-classical calcium phosphate mineralization at circum-neutral pH

Kathrin Schilling [a,*], Shaun T. Brown [b,c], Laura N. Lammers [c,d]

[a] Department of Earth Sciences, University of Oxford, South Parks Road, Oxford OX1 3AN, United Kingdom
[b] Department of Earth and Planetary Science, University of California, Berkeley, CA 94709, United States
[c] Energy Geosciences Division, E.O. Lawrence Berkeley National Laboratory, Berkeley, CA 94720, United States
[d] Department of Environmental Science, Policy and Management, University of California, Berkeley, 130 Mulford Hall, Berkeley, CA 94720, United States

Received 21 July 2017; accepted in revised form 11 August 2018; available online 22 August 2018

Abstract

Growth pathways of calcium (Ca) phosphate minerals are still under debate, but non-classical growth pathways, which encompass any mode of growth involving attachment of primary particles instead of monomer ions, are currently thought to dominate over classical mechanisms under a wide range of growth conditions. Cation desolvation during ion-by-ion growth is associated with the preferential uptake of isotopically light Ca in Ca-bearing phases, so the Ca isotope composition of Ca-bearing minerals can help to elucidate the dominant growth mechanism. Here, we combine stable Ca isotope analysis with mineralogical characterization and nanoscale imaging of growth features to determine for the first time the rate-dependent Ca isotope fractionation during seeded growth of hydroxyapatite (HAP) involving an octacalcium phosphate (OCP) precursor. Our data reveal that growth rates are strongly attenuated by pH, and that Ca isotope fractionation between the solid and growth solution is independent of growth rate between 1.9×10^{-9} and 2.8×10^{-8} mol Ca m^{-2} s^{-1}. Moreover, nanoscale images of surface topography reveal direct deposition of primary particles on the HAP seed surface following sustained growth, providing visual evidence of a non-classical growth pathway. Together, these findings support the hypothesis that hydroxyapatite growth is dominantly non-classical. The process of cluster nucleation from the bulk solution and attachment of these clusters to the seeded HAP apparently does not involve a significant kinetic isotope effect, which implies that abiogenically formed Ca-phosphates likely preserve the Ca isotope composition of the fluid from which the crystals originated.

Keywords: Ca-phosphate minerals; HAP; OCP; Non-classical growth; Cluster nucleation; Ca isotope fractionation; AFM; FT-IR

1. INTRODUCTION

Phosphorous (P) has been classified as a critical non-renewable resource (Elser and Bennett, 2011) and is a limiting nutrient in marine environments (*i.e.,* Tyrell, 1999; Elser et al., 2007). But over recent decades human activity has significantly increased P levels in surface waters leading to widespread eutrophication (*i.e.*, Daniel et al., 1998; Conley et al., 2009). Phosphate availability in marine ecosystems is determined by weathering of P-bearing rocks (Filippelli, 2008) and subsequent burial in sediments leading to the formation of phosphorite deposits, which are typically solid solutions of carbonated fluor- ($Ca_{10}(PO_4)_6F_2$) and hydroxy- ($Ca_{10}(PO_4)_6(OH)_2$) apatite end-members (Jahnke et al., 1983; Van Cappellen and Berner, 1989;

* Corresponding author.
E-mail address: kathrin.schilling@earth.ox.ac.uk (K. Schilling).

https://doi.org/10.1016/j.gca.2018.08.019
0016-7037/

Ruttenberg and Berner, 1993; Gunnars et al., 2004; Oxmann and Schwendenmann, 2014). Indeed, the apatite group of minerals includes the most stable, abundant, and biogeochemically essential Ca-phosphate phases (cf. Wang and Nancollas, 2008). Among the apatite group, hydroxyapatite (HAP) is of particular interest in material, biomedical, and environmental sciences (Dorozhkin, 2009; Hughes and Rakovan, 2015), because it forms vertebrate skeleton and tooth enamel (Fulmer et al., 1992, Palmer et al., 2008) and is an effective phase for the remediation of heavy metals (Seaman et al., 2001; Conca and Wright, 2006; Lammers et al., 2017) and radionuclides (Arey et al., 1998; Simon et al., 2008). Despite the critical role apatites play in the environment, formation pathways are debated (cf. Christoffersen et al., 1996; Christoffersen et al., 1998b; Onuma and Ito, 1998; Li et al., 2016a), and mechanistic models for the growth of apatite solid solutions are lacking. Better understanding of HAP growth mechanisms and corresponding stable isotope signatures in natural aqueous fluids are required to facilitate the development of predictive models of P fluxes in a variety of biogeochemical contexts both past and present, ranging from phosphorite formation to excess phosphorous mitigation and nutrient recovery and reuse.

In the geological context, apatite minerals regulate the formation of phosphorite deposits, control nutrient phosphate availability, and provide an important proxy for past ocean chemistry (*i.e.,* Guidry and Mackenzie, 2003; Filippelli, 2008; Hinojosa et al., 2012). The formation of authigenic apatite in marine sediments plays a key role in regulating nutrient orthophosphate availability and the marine cycling of P over geologic timescales (Guidry and Mackenzie, 2000; Ruttenberg, 2003; Filippelli, 2011), as it accounts for 50% of the global P burial (Ruttenberg, 2003). While it is clear that the pathways of apatite growth and formation are controlled by the fluid supersaturation with respect to different Ca-phosphate phases (*i.e.,* Wang and Nancollas, 2008), it is unknown whether authigenic apatite forms directly from supersaturated pore waters (Van Cappellen and Berner, 1989) or via a precursor octacalcium phosphate (OCP) phase (Jahnke et al., 1983; Gunnars et al., 2004; Oxmann and Schwendenmann, 2014). Developing an accurate reconstruction of the marine P cycle through geologic time will require a better understanding of the kinetic factors controlling apatite mineralization. Despite decades of research on the kinetics and mechanisms governing apatite growth processes, there is still limited consensus on the dominant growth pathway for these Ca-phosphate phases.

Both classical (Nancollas and Koutsoukos, 1980; Christoffersen and Christoffersen, 1992; Christoffersen et al., 1998a, 1998b; Li et al., 2016a) and non-classical (e.g., Onuma et al., 1995, 1996; Onuma, and Ito 1998; Kanzaki et al., 2001; Wang et al., 2012; Habraken et al., 2013; De Yoreo et al., 2015; Li et al., 2016a) mechanisms have been proposed to explain observed HAP growth kinetics. Classical crystal growth is characterized by the attachment of ionic monomers to active growth sites, especially steps and kinks, on the crystal surface (cf. De Yoreo et al., 2015) and can occur at very low supersaturation due to the presence of defects that terminate at the crystal surface (Burton et al., 1951). This mechanism is supported by evidence from bulk crystallization experiments that HAP growth may be rate-limited by the dehydration of Ca^{2+} ions and by water hydrolysis during incorporation of OH^- into the crystal (Christoffersen and Christoffersen, 1992; Christoffersen et al., 1998a, 1998b). The feasibility of this mechanism has also been confirmed by visual evidence of classical growth features (*i.e.*, spiral hillocks) at the HAP {1 0 0} surface (Li et al., 2016a). At higher supersaturations, however, the free energy barrier to nucleation becomes sufficiently low to enable formation of primary particles that can aggregate or deposit on the growth surface (Niederberger and Cölfen, 2006), leading to non-classical crystallization by particle attachment (CPA). Several classes of geochemically important minerals, including metal oxides, sulfides, and phosphates, have been shown to grow via CPA under certain conditions (Onuma et al., 1995; Onuma and Ito, 1998; Onuma, 2006; Habraken et al., 2013; De Yoreo et al., 2015).

Nanoscale imaging of active HAP growth using in-situ Atomic Force Microscopy (AFM) has shown that classical growth and non-classical particle attachment can occur simultaneously, but the attachment of primary particles likely dominates the overall HAP growth over a wide range of supersaturations (Onuma et al., 1995; Li et al., 2016a). Several additional indirect lines of evidence support a CPA growth pathway for HAP. Step heights on the active growth surface (~0.8 nm) exceed the molecular unit width of 0.24 nm for PO_4^{3-} (Onuma et al., 1995, 1996), and the kinetic coefficient for growth unit attachment to steps (*i.e.*, the step kinetic coefficient, β_{st}) under physiological conditions (pH 7.4) is ~100 times smaller than for similar ionic minerals (Onuma, 2006). Primary particles of uniform size between 0.7 and 1.0 nm have been identified by both dynamic light scattering and AFM in HAP-supersaturated solution experiments (Onuma and Ito, 1998; Wang et al., 2012), and *ab initio* calculations identified stable isomers of the proposed growth unit, "Posner's cluster," which is also ~0.8 nm in diameter (Posner and Betts, 1975; Onuma and Ito, 1998; Kanzaki et al., 2001; Yin and Stott, 2003; Li et al., 2016a). In addition, HAP growth is known to involve the formation of precursor phases, including octacalcium phosphate (OCP; $Ca_8(HPO_4)_2(PO_4)_4.5H_2O$), brushite ($CaHPO_4.2H_2O$; Johnsson and Nancollas, 1992; Wang and Nancollas, 2008) and in some cases amorphous Ca-phosphate (ACP; $Ca_xH_y(PO)_z.nHO$, n = 3–4.5; Wang and Nancollas, 2008) at very high supersaturations (Habraken et al., 2013). In natural systems, the dominance of a non-classical pathway is evidenced by the fact that growth of HAP appears not to occur at all in solutions that are supersaturated with respect to HAP but undersaturated with respect to OCP (Jahnke et al., 1983; Van Cappellen and Berner, 1989; Koutsoukos, 1998; House, 1999; Gunnars et al., 2004; Rokidi et al., 2011).

Although these studies present a compelling case for a dominantly non-classical crystal growth mechanism for HAP, none of this evidence can conclusively rule out the importance of direct ion attachment to the growth surface

and the overall growth rate. Stable Ca isotopes can be used as tracers of molecular phenomenology if the processes controlling kinetic isotope fractionation are understood. The attachment of Ca^{2+} ions during surface-controlled mineral growth is associated with a kinetic isotope effect that is thought to arise due to the faster rate of dissociative metal ion desolvation of the light isotopologue (Hofmann et al., 2012; Colla et al., 2013). This phenomenon leads to the preferential uptake of lighter isotopes of Ca during classical growth of calcite, generating a rate-dependent range in solid-aqueous fractionation factors ($\Delta^{44/40}Ca_{s\text{-}f} = \delta^{44/40}Ca_{solid} - \delta^{44/40}Ca_{fluid}$) between −0.5‰ and −2‰ (Skulan and DePaolo, 1999; Gussone et al., 2003; DePaolo, 2004; Lemarchand et al., 2004; Tang et al., 2008).

Although the kinetic isotope effect associated with classical HAP precipitation has not been directly determined, we assume that both the rate dependence and preferential incorporation of the isotopically light Ca are indicative of a classical growth process that is rate limited by dissociative metal desolvation, as evidenced in the Ca-minerals calcite and gypsum (Nielsen et al., 2012; Harouaka et al., 2017). Non-classical growth of Ca phosphate minerals, on the other hand, is thought to be controlled by the formation, assembly, and deposition of Ca orthophosphate ion pairs and prenucleation clusters, especially $Ca(HPO_4)_3^{4-}$ (Habraken et al., 2013). In this case, stable isotope fractionation between aqueous solution and the precipitating solid is unlikely to be rate limited by Ca desolvation, but rather by equilibrium aqueous speciation if complex formation and dissociation are rapid relative to aggregation. Rate-dependent isotope fractionation may occur if diffusive transport of either free Ca^{2+} aquo-complexes or Ca orthophosphate complexes is rate-limiting; however, the magnitude of this effect is likely to be small compared to kinetic isotope fractionation arising from dissociative Ca desolvation (Bourg et al., 2010; Hofmann et al., 2012). Early measurements of the Ca isotope budget in vertebrates suggested a characteristic $\Delta^{44/40}Ca_{s\text{-}f}$ of −1‰ arising from skeletal HAP biomineralization (Skulan and DePaolo, 1999), which is similar to the Ca isotope fractionation signature observed during calcite growth. However, Ca isotope fractionation during the growth of synthetic Ca-phosphate minerals in the absence of vital effects has not been previously studied.

Here, we combine nanoscale AFM imaging with measurements of the Ca isotope fractionation factor ($\Delta^{44/40}Ca_{s\text{-}f}$) over a range of Ca-phosphate growth rates to investigate the dominant mechanism of HAP growth. Seeded constant-composition precipitation experiments were performed under varied aqueous supersaturation at circum-neutral pH in stirred a mixed-flow reactor. Solid precipitates were analyzed for mineralogy and elemental and Ca isotope composition. The elemental concentrations of the effluent from the stirred mixed-flow reactor were used to determine precipitation rates. Overgrowth on the HAP seed material was imaged ex-situ using AFM to characterize growth features. Combing results from all these analytical techniques, our approach aims to improve the understanding of HAP formation mechanisms and associated stable Ca isotope effects in biological, geological, and engineered systems.

2. MATERIALS AND METHODS

2.1. Synthesis of HAP seed material

A well-crystallized HAP seed material was synthesized using the aqueous phase method adapted from Koutsopoulos (2002) followed by molten salt recrystallization at high temperature (cf. Tas, 2001). For the aqueous synthesis, we prepared 500 ml of 0.3 M H_3PO_4 from an 85% phosphoric acid stock solution (Sigma Aldrich) and 500 ml of 0.5 M $Ca(NO_3)_2$ in double deionized water (DDI, 18mΩ system). Both solutions were purged with N_2 and their pHs were brought above 10 by adding 1 M KOH before starting the synthesis. The synthesis was carried out at a flow rate of ~1.5 mL min^{-1} under continuous stirring and N_2-purging. During the synthesis, the pH of the mixed solution was kept between 9 and 10 by manual addition of KOH. After both solutions were completely added, the synthesized HAP crystals were filtered and washed with DDI water. The synthesized nano-sized HAP crystals were then recrystallized to generate μm-sized HAP crystals in a molten salt solution of K_2SO_4 following the procedure reported by Tas (2001). Briefly, the nano-sized HAP was mixed well with K_2SO_4 at a 1.6:1 weight ratio of K_2SO_4 to HAP using mortar and pestle. The resulting mixture was placed in an alumina crucible and calcined at 1190 °C for 5 h and removed to cool. Once cooled, the HAP crystals were separated by repeatedly suspending the salt mixture in DDI water until specific conductance did not exceed 2.4 μS/cm.

2.2. Calcium phosphate growth experiments

Growth experiments were conducted in a stirred mixed-flow reactor (UHP-43, Cole Parmer) with a fluid reservoir of 70 ml (Fig. 1). The top and bottom of the reactor were closed by caps with O-rings. Separate Ca- and (T_{Ca} solution) P-bearing (T_P solution) influent solution were pumped into the top of the reactor via a Y-connector (Fig. 1). To ensure continuous mixing of the reservoir fluid and the HAP seed material, the reactor was equipped with a PTFE stir bar attached to the top cap of the reactor vessel. The reactor effluent flowed through a 0.45 μM nitrocellulose filter and glass fiber filter at the bottom of the reactor.

For each experiment, we ensured that ionic strength, the concentration and activity of the Ca^{2+} ions and phosphate species, and the saturation index maintained a steady-state. Influent solutions were prepared using reagent grade $CaNO_3$ (BioXtra, 99%, Sigma Aldrich) and KH_2PO_4 (99.99% trace metal grade, Sigma Aldrich) in DDI water. All experiments were performed at a fixed ionic strength of 0.1 M by adding KNO_3 to the T_{Ca} solution. The experiments were conducted at pH values ranging from of 6.5 to 7.1 as pH controls aqueous orthophosphate speciation (Fig. 2) and supersaturation with respect to various Ca-phosphate phases (Table 1). The pH of the solutions was adjusted accordingly using 1 M KOH (99.97% trace metal grade, Sigma Aldrich) and measured with a Thermo Orion Versa Star Pro pH meter equipped with a Beckman Coulter pH electrode (accuracy of ±0.01). The electrode

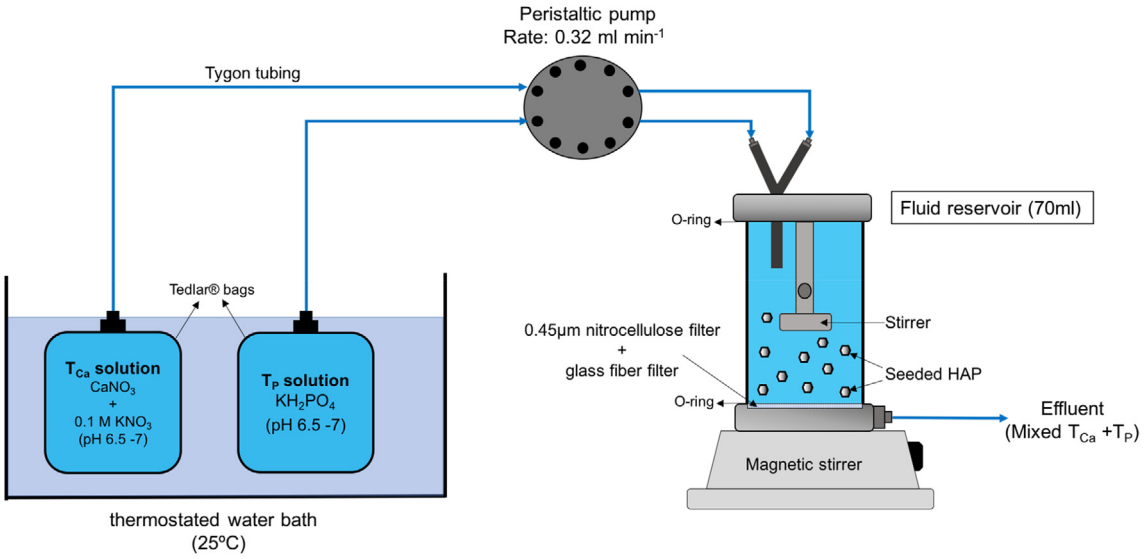

Fig. 1. Schematic of the experimental setup showing the stirred mixed-flow reactor (right) and Tca + Tp solutions (water bath at 25 °C) supply imposed by a peristaltic pump.

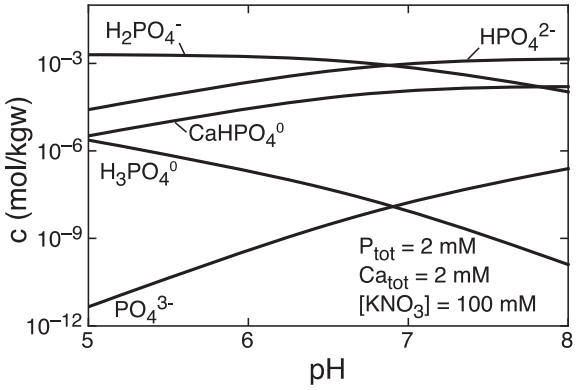

Fig. 2. Aqueous dissolved inorganic P species.

was calibrated using buffer solutions of pH 4, 7 and 10. Both T_{Ca} and T_P solutions were purged with N_2 and each solution was transferred to 5 L Tedlar bags (Sigma Aldrich) to prevent exchange of the solutions with atmospheric CO_2 during the experiment. The Tedlar bags with the solutions were stored in a thermostated water bath at 25 °C. To initiate crystal growth, 0.2 ± 0.02 g of HAP seed material was added to the mixed-flow reactor. The crystal growth was sustained by continuously adding T_{Ca} and T_P solutions in a 1:1 ratio to the reactor vessel at constant flow rate of 0.32 ml min^{-1} using a peristaltic pump. The effluent (mixed $T_{Ca} + T_P$) was collected over a period of one day (24 h) or two weeks in 15 ml centrifuge tubes over the first 24 h via a fraction collector (Pharmacia LBK Fraction Collector FRAC 200) in 15 min intervals and then manually in 500 ml Nalgene bottles every 24 h. The pH, Ca and P concentrations of the effluent were periodically measured to ensure steady-state conditions in each experiment. The effluent was acidified with concentrated HNO_3 to stop further nucleation and precipitation of the Ca-phosphates outside the reactor. After completion of the experiment (24 h or 2 weeks), the final solids were recovered from the reactor, dried at 60 °C for 48 h and weighed to confirm an increase in mass relative to the initial HAP seed material. Final masses are not a reliable indicator of total growth and are not reported, because not all µm-size HAP material could be recovered from the reactors.

2.3. Characterization of precipitated HAP solids

Bulk solid phase mineralogy of seed HAP and solid material precipitated in the reactor was determined using powder X-ray diffraction (XRD), Fourier-transform infrared spectroscopy (FT-IR), and by measurement of major elemental composition of the precipitated solids. XRD analyses were carried out using PANalytical X'Pert Pro diffractometer equipped with alpha Co Ka radiation source at 40 kV and 40 mA, step scanning from 3 to 100° 2 Theta and a step size of 0.017°. All XRD spectra were background-corrected and analyzed using PANalytical's X'Pert HighScore Plus software, which is based on the profile refinement method by Rietveld (1969).

FT-IR spectra (Thermo Nicolet 6700) were obtained by mixing about 10 mg HAP with 1 g of powdered potassium bromide. Using a Mini Arbor KBr desktop pellet press the mixture was compressed to a pellet for 30 seconds or until transparent. The infrared scanning was performed in absorbance mode at mid-infrared range of 4000 and 400 cm^{-1} with a resolution of 4 cm^{-1}. For the 1-day experiments (CaP-4 and 5), XRD and FT-IR analysis were not conducted as the amount of growth was very small and thus solid overgrowth mineralogy was most likely superimposed by the HAP seed material.

The surface topography and nanoscale growth features of the seed material and precipitated overgrowth were characterized by ex-situ AFM performed on a Multimode-8 (Bruker AXS, Co). For the AFM technique, solids were

Table 1
Concentrations of Ca and P input solution, initial pH and average pH, saturation state (logΩ) with respect to HAP and OCP, initial amount of HAP as seed material, mass of solids after experiments and duration of the experiment. All experiments were performed at a total ionic strength of 100 mM using KNO_3. Growth rates are determined from the Ca isotope double spike concentrations given in Table 2.

Exp.	pH steady-state	Ca ($\times 10^{-3}$ M)[a]	P ($\times 10^{-3}$ M)	logΩ HAP[b]	logΩ OCP[c]	Rate (mol Ca m^{-2} s^{-1}) [± err.]	Rate HAP (mol HAP m^{-2} s^{-1}) [± err.]	Rate OCP (mol OCP m^{-2} s^{-1}) [± err.]	Ca:P (mol/mol overgrowth) [± err.]	XRD mineralogy	FT-IR bands	Duration (days)
CaP-1	6.94	1.90 ± 0.07	1.06 ± 0.04	8.18 ± 0.67	2.46 ± 0.4	2.0×10^{-9} [1.02×10^{-9}]	4.0×10^{-10} [5.5×10^{-10}]		1.36 ± 0.06	HAP, OCP	3600–3200, 1103, 1022, 902, 602, 560	14
CaP-2	7.07	1.06 ± 0.02	0.63 ± 0.03	6.24 ± 0.64	−0.93 ± 0.6	1.93×10^{-9} [5.9×10^{-10}]	3.9×10^{-10} [5.4×10^{-10}]		1.77 ± 0.29	HAP	3600–3200, 1100, 914, 902, 628, 602, 563	13
CaP-3	6.97	1.27 ± 0.03	0.73 ± 0.04	5.97 ± 0.56	−0.97 ± 0.5	2.64×10^{-9} [5.9×10^{-10}]	5.3×10^{-10}		1.38 ± 0.07	HAP	3600–3200, 1238, 1100, 902, 632, 602, 559	14
CaP-4	6.59	4.08		8.55 ± 0.53	4.28 ± 0.4	1.56×10^{-8} [2.4×10^{-9}]		1.9×10^{-9} [3.4×10^{-10}]	nd	nd	nd	1
CaP-5	6.53	2.87 ± 0.24	1.70 ± 0.12	7.47 ± 0.96	2.43 ± 1.0	1.64×10^{-8} [1.8×10^{-9}]		2.1×10^{-9} [3.5×10^{-10}]	nd	nd	nd	1
CaP-6	6.80	2.65 ± 0.29	1.45 ± 0.18	6.72 ± 0.64	1.08 ± 0.7	2.76×10^{-8} [1.4×10^{-9}]		3.5×10^{-9} [3.3×10^{-10}]	1.40 ± 0.23	HAP, OCP	3600–3200, 1103, 1026, 902, 602, 563	13
CaP-7	6.69	2.63 ± 0.19	1.62 ± 0.22	7.50 ± 0.70	2.21 ± 0.8	2.05×10^{-8} [1.38×10^{-9}]		2.6×10^{-9} [3.4×10^{-10}]	1.63 ± 0.39	HAP, OCP	3600–3200, 1103, 1022, 902, 602, 559	15
CaP-8	6.59	2.35 ± 0.15	1.43 ± 0.13	6.75 ± 0.88	1.16 ± 1.0	1.82×10^{-8} [1.34×10^{-9}]		2.3×10^{-9} [3.3×10^{-10}]	1.27 ± 0.28	HAP, OCP	3600–3200, 1103, 1022, 902, 602, 559	14
Seeded HAP									1.65 ± 0.29	HAP	3568, 1049, 980, 602, 559	

[a] Derived from double-spike Ca isotope.
[b] Ksp for HAP = 3.98×10^{-59} after Wang and Nancollas (2008).
[c] Ksp for OCP = 2.51×10^{-97} after Wang and Nancollas (2008).

mounted on a metal disc using thermal wax (Quick-Stick 135, Electron Microscopy Sciences). Ex-situ AFM images were collected on the {1 0 0} face at the quantitative nanomechanical mode (peak-force QNM). For all AFM images, we used a silicon nitride cantilever (SNL-10) with a spring constant of 0.35 N/m and a radius of the tip curvature of 2 mm. Crystal morphology and particle size estimates were imaged using scanning electron microscopy (SEM, Hitachi TM-1000, operating at 15 kV acceleration voltage) on HAP solids mounted on carbon-adhesive tape.

Bulk elemental compositions of Ca and P in the final solids were determined by completely digesting 20 mg of the recovered solid material in 2 ml of concentrated HNO_3. When solid material was visibly dissolved, 18 ml of DDI water were added and Ca and P concentrations were measured using inductively coupled plasma-optical emission spectroscopy (ICP-OES; see below). As this material includes both seeded HAP and overgrowth, the Ca/P ratio of overgrowth material was determined by subtracting the seed composition from the bulk solid.

2.4. Ca concentration and isotope analysis of fluid and solids

Dissolved Ca and P in the reactor effluent were measured by ICP-OES (Perkin Elmer 5300 DV) equipped with GemCone nebulizer and cyclonic spray chamber. All samples were diluted (1:50) in 2% HNO_3. Solutions for five-point calibration were gravimetrically prepared in 2% HNO_3 from certified single element ICP Certipur standards (Merck Millipore). The prepared standard solutions ranged between 1–6 mg L^{-1} for Ca and 0.5–3 mg L^{-1} for P. For data quality assurance, we used an internal standard (scandium 5 mg L^{-1}) and analyzed a quality control standard (Ca, 4 mg L^{-1}; P, 2 mg L^{-1}) after every 10 samples with an acceptance criterion of ±10%. The relative uncertainties were 7.8% for Ca and 5.5% for P based on repeated check standard measurements (n = 12).

The Ca isotope ratios and precise elemental Ca concentrations were measured with Finnigan TRITON thermal ionization mass spectrometer (TIMS). For Ca isotope analysis, we used the double spike method ($^{42}Ca + {}^{48}Ca$). Calcium separation was performed with Ca-specific DGA resin (Eichrom) using 250–300 µl resin volume (Horwitz et al., 2005). The columns were rinsed with 1 mL of each DDI water, 3 N HNO_3, deionized H_2O, 6 N HCl and DDI water followed by a final 0.5 mL rinse with 3 N HNO_3. The spiked sample re-dissolved in 100 µL 3 N HNO_3 was loaded on the column and subsequently rinsed with 100, 300 and 500 µL of 3 N HNO_3. In the last step, 1.5 mL of DDI water was stepwise added to elute Ca from the column. The purified Ca sample was loaded on zone-refined Re double filaments. All Ca isotope ratios are expressed in the delta notation as $\delta^{44/40}$Ca (‰) relative to bulk silicate earth (BSE) with a $^{44}Ca/^{40}Ca$ value of 0.0212035:

$$\delta^{44/40}Ca = \left(\frac{\left({}^{44}Ca/{}^{40}Ca \right) sample}{\left({}^{44}Ca/{}^{40}Ca \right) BSE} \right) \times 1000. \quad (1)$$

The NIST SRM 915a reference material was analyzed several times for each sample turret and used to determine external errors on $\delta^{44/40}$Ca on samples measured during the study period. The NIST SRM915a is with an average value of −1.00‰ (n = 21) within the range of previously reported values (Gussone et al., 2003; Amini et al., 2009; Holmden et al., 2012). The external 2σ reproducibility of $\delta^{44/40}$Ca for NIST SRM915a was ±0.18‰ (n = 21), and the analytical uncertainty on the double spike Ca concentration is estimated to be 1%. The external 2σ reproducibility for $\delta^{44/40}$Ca based on replicate sample measurements was 0.15‰ (n = 13).

2.5. Determination of growth rate and $\Delta^{44/40}Ca_{s\text{-}f}$ as function of supersaturation

To calculate the chemical speciation of the initial bulk solutions we used PHREEQC (version 3.1.7-9213) and the llnl.dat database originated from thermo.com.V8.R6.230. Supersaturation was calculated as:

$$S_{Ca/P} = log\left(IAP/K_{sp}\right) \quad (2)$$

where IAP is the ion activity product and K_{sp} is the solubility constant for HAP equal to 3.98×10^{-59} for the reaction $Ca_5(PO_4)_3(OH) \rightarrow 5\ Ca^{2+} + 3\ PO_4^{3-} + OH^-$ (Wang and Nancollas, 2008) or for OCP equal to 2.51×10^{-97} for the reaction $Ca_8H_2(PO_4)_6.5H_2O \rightarrow 8\ Ca^{2+} + 6\ PO_4^{3-} + 2\text{-}H^+ + 5\ H_2O$ (Fernandez et al., 1999).

Ca-phosphate growth rates cast in terms of net Ca uptake (R_{Ca}, mol Ca s^{-1}) were calculated,

$$R_{Ca} = (c_{t0} - c_{tx}) \times Q \quad (3)$$

where c_{t0} represents the molar concentration of Ca in the influent solution and c_{tx} is the mean Ca concentration of the fluid reservoir effluent at all sampling points taken 24 h or more into the experimental period under flow rate Q (L s^{-1}), using Ca concentrations determined from the double spike method. Surface area normalized growth rates are reported assuming a constant value of specific surface area equal to that of the seed material added at the beginning of the experiments (0.672 m^2/g); however, for the high supersaturation experiments we expect this to significantly underestimate the true reactive surface area due to crystal nucleation.

The Ca isotope composition of the overgrowth material was determined from the $\delta^{44/40}$Ca of the HAP seed material and the collected final solids, which is a mixture of the seed plus precipitates formed during the experiment. The fraction of final solids precipitated during each experiment (f_{precip}) was determined from the total moles of Ca precipitated in an experiment of duration Δt $\left(n_{precip} = R_{Ca}\Delta t\right)$,

$$f_{precip} = \frac{n_{precip}}{n_{precip} + n_{seed}} \quad (4)$$

The Ca isotope composition of the precipitate ($\delta^{44/40}Ca_{precip}$) was determined from Eq. (1) using the calculated solid Ca isotope ratio of the precipitate,

$$\left({}^{44}Ca/{}^{40}Ca\right)_{precip} = \left[\left({}^{44}Ca/{}^{44}Ca\right)_{sample} - \left(1 - f_{precip}\right) \times \left({}^{44}Ca/{}^{44}Ca\right)_{seed}\right]/f_{precip} \quad (5)$$

The Ca isotope fractionation factor between the solid and aqueous solution during growth ($\Delta^{44/40}Ca_{s\text{-}f}$) was calculated as the difference between the precipitated material and the Ca isotope composition of the reactor effluent ($\delta^{44/40}Ca_{aq,eff}$),

$$\Delta^{44/40}Ca_{s-f} = \delta^{44/40}Ca_{precip} - \delta^{44/40}Ca_{aq,eff} \quad (6)$$

An alternative value of the Ca isotope fractionation factor was calculated based on the difference in the aqueous $\delta^{44/40}$Ca in the influent and the effluent solutions ($\Delta^{44/40}Ca_{fluid}$). Formal error propagation was used to determine the uncertainty on the growth rate, $\delta^{44/40}Ca_{precip}$, and $\Delta^{44/40}Ca_{s\text{-}f}$ values.

3. RESULTS

3.1. Mineralogy and nanoscale surface structure of precipitated calcium phosphates

The bulk elemental compositions of the final solids were determined to provide a first order constraint on the overgrowth mineralogy. The Ca/P ratios of the final solids are lower than those of the input fluid and the seeded HAP (Ca/P = 1.65 ± 0.29), suggesting the precipitation of either

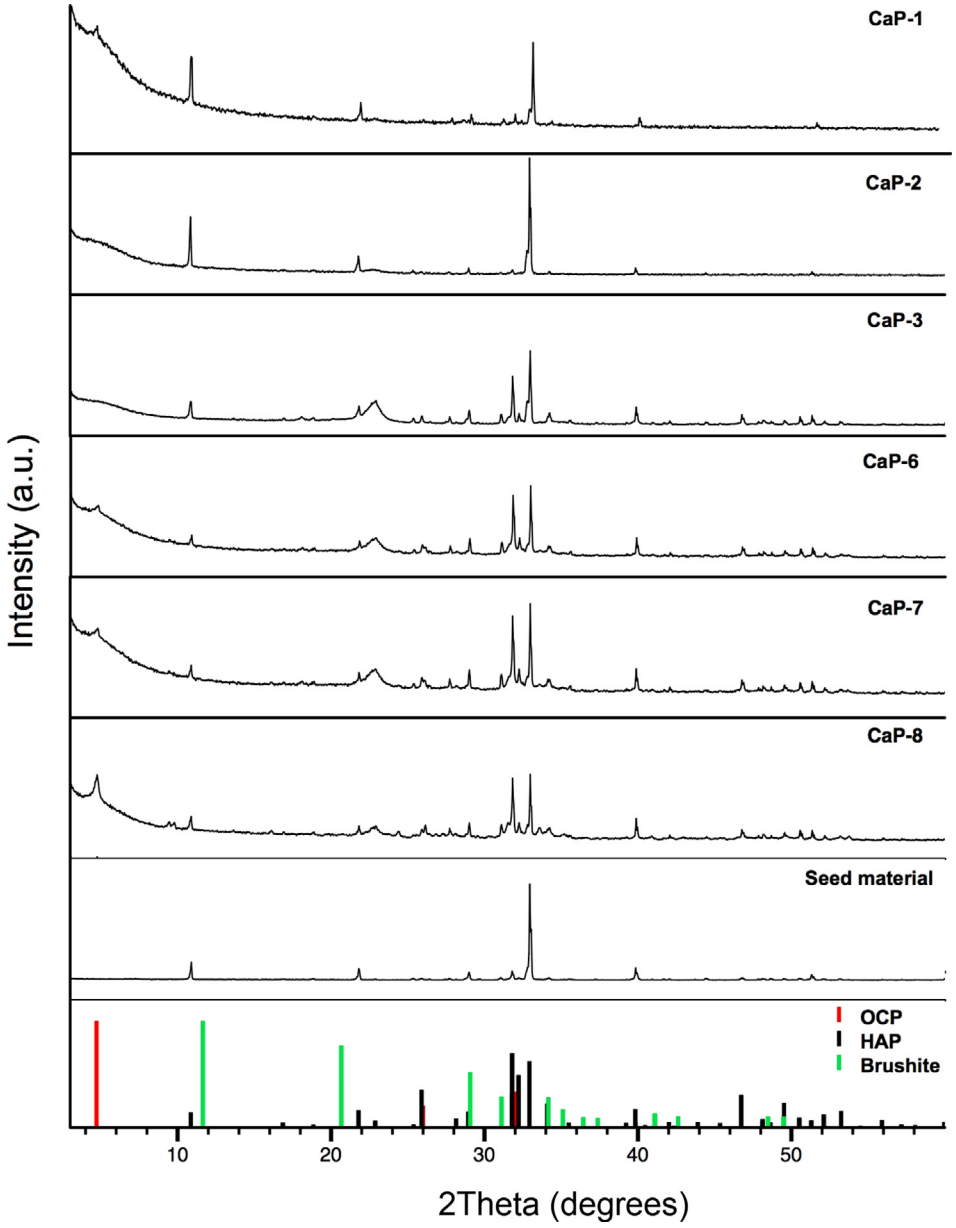

Fig. 3. XRD pattern of the seeded HAP and the final HAP phases after 13–15 days growth experiments. Lower panel shows the typical XRD peaks for HAP (black), OCP (red) and brushite (green). (For interpretation of the references to colour in this figure legend, the reader is referred to the web version of this article.)

OCP or Ca-deficient HAP. Formation of an admixture of OCP and HAP is supported by our XRD results. All final solids contain the dominant HAP reflections at 10.8, 31.8, 32.2 and 32.9° (Fig. 3; JCPDS 09-0432), originating at least in part from the seed material added to the reactor. OCP formation occurs in the experiments CaP-6, 7 and 8 where X-ray diffraction of final solids (Fig. 3) show the characteristic reflection of OCP at 4.7° {100} (JCPDS 26-1056). The absence of the typical OCP peak for the final solids from the experiments CaP-1, 2 and 3, which are undersaturated with respect to OCP (Table 1), supports the formation of predominantly HAP.

The FT-IR spectra of the final solids show modified bands compared to the seed material (Table 1 and Fig. 4). Consistent with our XRD observations, we do not detect the distinctive peak band for brushite (985 cm^{-1}) or amorphous calcium phosphates (ACP; singular band for P—O bonds at 600–560 cm^{-1}) for any of the final solids. Small additional bands at ~1100 and 1238 cm^{-1} for the final solid suggest the incorporation of small amounts of CO_3^{2-} or HPO_4^{2-}.

There are distinct differences in morphology of the final solids and the seeded HAP (Figs. 5–7). The SEM images indicate that the final solids include particles much smaller in size (sub-μm) than the hexagonal μm-sized HAP seed material (Fig. 5). High resolution surface features of ex-situ AFM images show the direct deposition of nuclei on the growth surface (Fig. 6b–h). Measured transects of relief heights for the final solids correlate with aqueous supersaturation with respect to HAP (Fig. 6), even when OCP growth is observed (Fig. 2). Relief heights and roughness vary between 8 and 25 nm and 6.2 and 7.7 nm, respectively (Fig. 7). For the experiment with the highest supersaturation ($\log\Omega_{OCP} = 4.3$ and $\log\Omega_{HAP} = 8.6$; CaP-4; Table 1), we observe the largest 3-D structural features with heights of ~25–36 nm (Fig. 6b). In contrast, surface features with

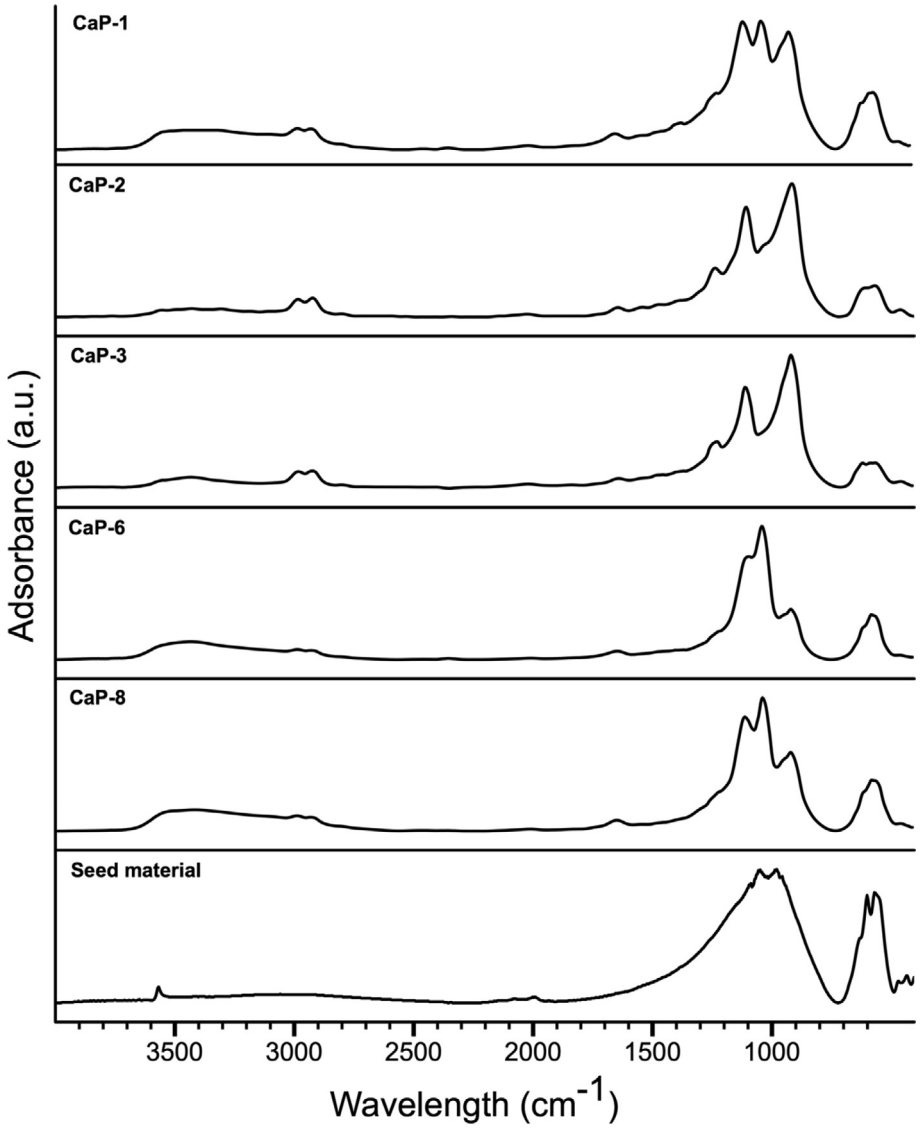

Fig. 4. FTIR spectra of precipitated calcium phosphate and seed material.

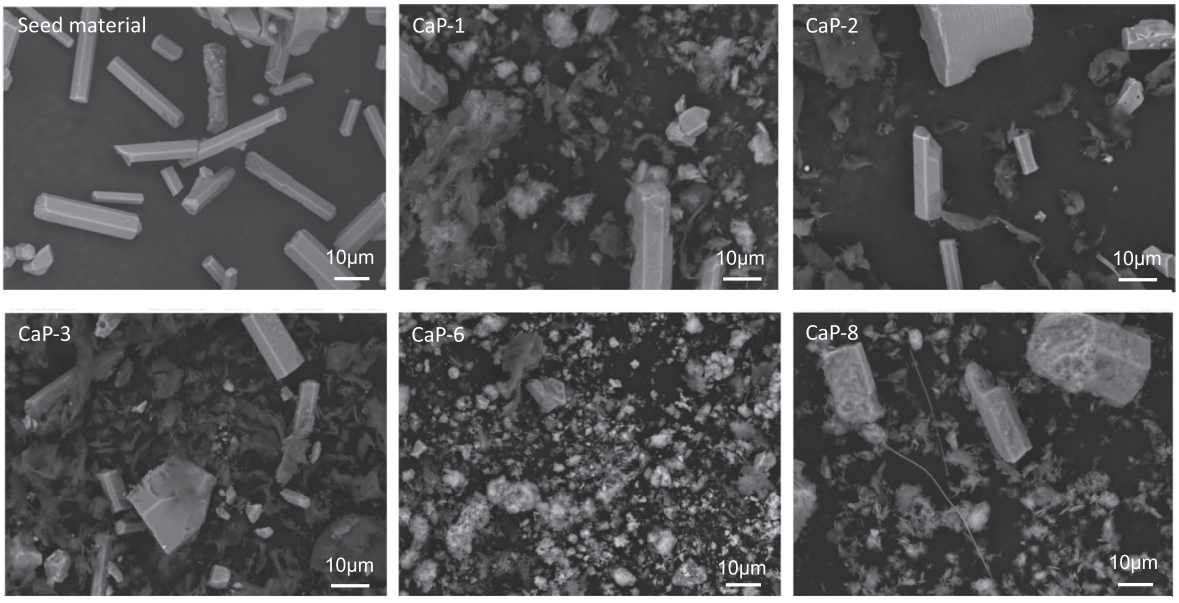

Fig. 5. SEM images of the HAP seed material and the final solids of the growth experiments.

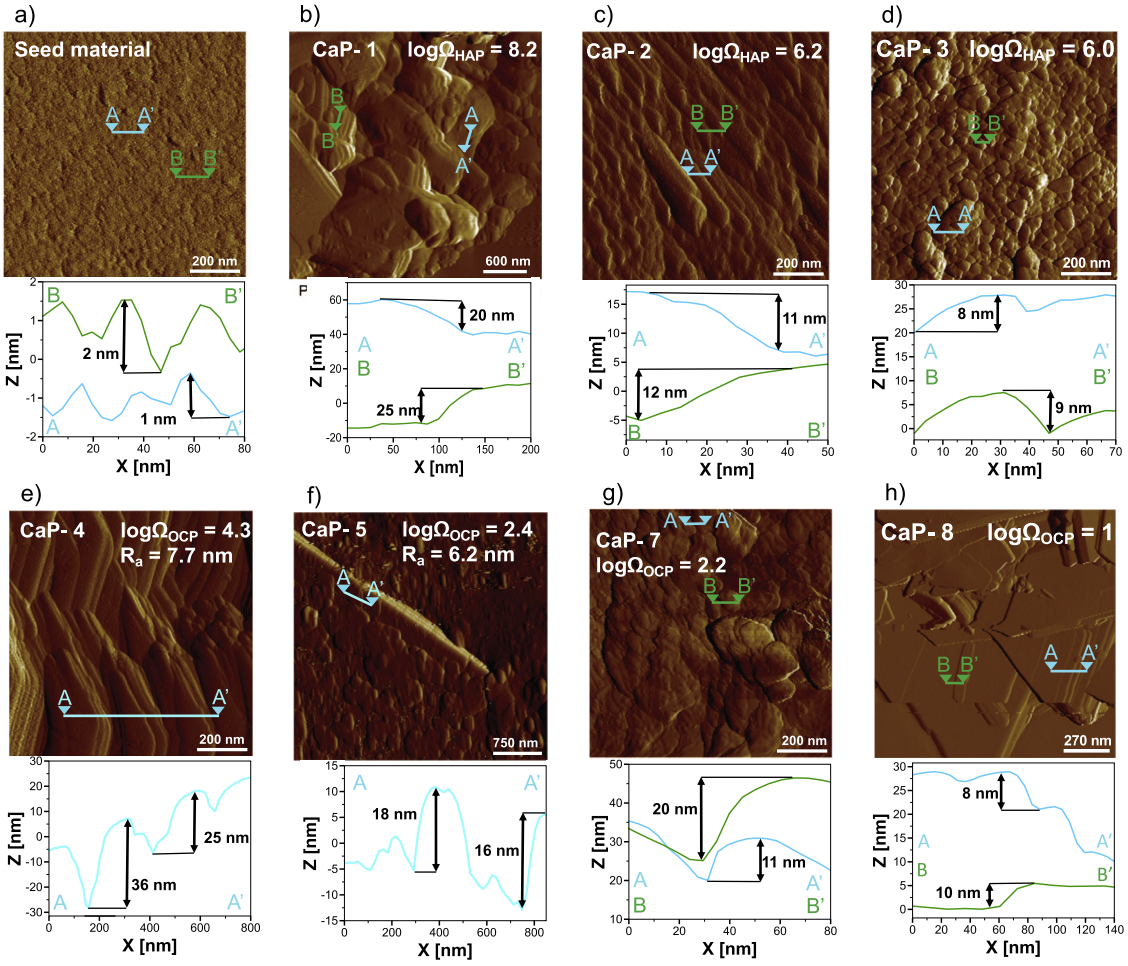

Fig. 6. AFM deflection images in QNM mode (a–f) of the surface morphology for the {100} face of cHAP surface under different condition of supersaturation after 1 day (CaP-4 and CaP-5) and 13–15 days (CaP-1-3 and CaP-7, 8). Height profiles of HAP surfaces are examined along the light blue and green lines. (For interpretation of the references to colour in this figure legend, the reader is referred to the web version of this article.)

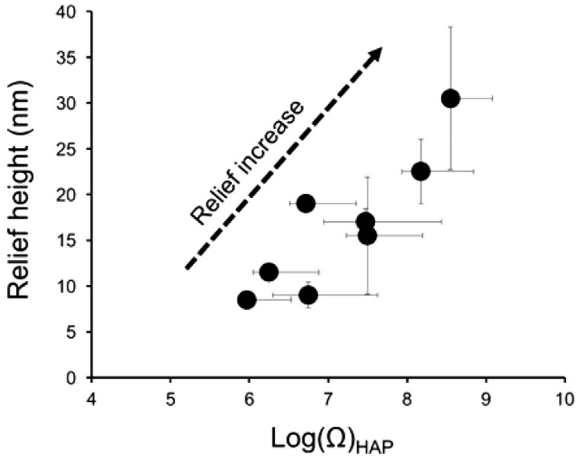

Fig. 7. Change in surface morphology expressed as average relief heights (nm) as a function of supersaturation (log(Ω)). The relief heights are derived from the transect present in Fig. 2b–h. Error bars for *x*-axis represent the absolute error on log(Ω) derived from minimum and maximum Ca and P concentrations. Error bars of *y*-axis represent the deviation (1-sigma) from the height measurements in Fig. 2.

only 8–9 nm in heights occur at the lowest growth rates (2.6×10^{-9} mol Ca m^{-2} s^{-1}; CaP-3).

3.2. Precipitation kinetics

For the experiments conducted at steady-state pH of ~7, we only observe the formation of HAP, while experiments with pH values ranging between 6.5 and 6.9 also show the formation of the precursor phase OCP (Table 1). The fastest growth rates accompanied with OCP formation occurs at the lowest steady-state pH value (Table 1). For the experiments with formation of OCP (CaP-4 to CaP-8), the growth rates range between 1.6×10^{-8} and 2.8×10^{-8} mol Ca m^{-2} s^{-1}. For the two experiments with predominant formation of Ca-deficient HAP as supported by our XRD data (CaP-2 and 3), the growth rates are 1.9 and 2.6×10^{-9} mol Ca m^{-2} s^{-1}, which are up to one-order of magnitude slower than observed for OCP growth (Table 1). For experiment CaP-1 we have several lines of evidence to assume that only HAP is formed although the growth solution is supersaturated in respect to OCP ($\log\Omega_{OCP} = 2.46$). First, the slow growth rate of 2×10^{-9} mol Ca m^{-2} s^{-1} is within in the range of growth rates observed for HAP in our study. Secondly, the XRD pattern for CaP-1 lacks the characteristic {100} peak for OCP (Fig. 3).

3.3. Ca isotope data and $\Delta^{44/40}Ca_{s\text{-}f}$

The results of Ca isotopic composition of the bulk solution and final solids are listed in Table 2. The Ca isotopic composition of the bulk solution in the fluid reactor ($\delta^{44/40}Ca = 0.31 \pm 0.16$‰, 1σ) shows no significant variation over the duration of the experiment and is isotopically identical to the Ca influent solution ($\delta^{44/40}Ca = 0.25 \pm 0.24$‰). During the relative short residence time (~4 h) of the bulk solution in the reactor, only 0.7 to 12 mol % Ca is removed from the bulk solution by the formation of Ca-phosphates. Thus, potential isotopic shifts are difficult to detect in the bulk solution because of the slow growth rates of 10^{-8} to 10^{-9} mol Ca m^{-2} s^{-1} (0.003 to 0.05 mol Ca s^{-1} in the fluid reservoir). The mean Ca isotopic composition of the final solids ($\delta^{44/40}Ca = 0.23 \pm 0.12$‰) is nearly identical to Ca isotopic composition of the seeded HAP ($\delta^{44/40}Ca = 0.23 \pm 0.22$‰) and is also statistically identical to the bulk solution ($\delta^{44/40}Ca = 0.31 \pm 0.16$‰, $p = 0.19$). Based on these average solid and solution values, we estimate a Ca isotope fractionation factor between the solid and aqueous solution for synthetic HAP and/or OCP to be $\Delta^{44/40}Ca_{s\text{-}f} = -0.08 \pm 0.21$‰ (1σ).

The $\Delta^{44/40}Ca_{s\text{-}f}$ values determined from the final solids range between -0.94 ± 1.97‰ and 0.84 ± 2.08‰ (2σ) for HAP and -0.73 ± 3.06‰ and 0.74 ± 3.00‰ (2σ) for the OCP overgrowth, with an average value of $\Delta^{44/40}Ca_{s\text{-}f} = 0.00 \pm 0.69$‰ (1σ; Fig. 8 and Table 3). These large ranges are characteristic of the shortest duration (experiments CaP-4 and CaP-5) and slowest growth rate experiments (experiments CaP-1 through -3), which have large magnitude uncertainty due to the very small amount of overgrowth material precipitated relative to the total seed. Based on the $\delta^{44/40}Ca$ values of the bulk solution, the calculated $\Delta^{44/40}Ca_{s\text{-}f}$ vary between -3.1 ± 2.1‰ and 0.40 ± 0.78‰ (2σ; Fig. 8 and Table 3). The large uncertainties on our fluid-derived $\Delta^{44/40}Ca_{s\text{-}f}$ data for the HAP overgrowth are due the extremely small shift in Ca concentrations relative to the initial bulk solution. This results in errors associated with slower growth experiments that are much larger than the analytical uncertainty on $\delta^{44/40}Ca_{sample}$ (*i.e.*, ±0.2‰, 2σ internal reproducibility). Thus, in future even longer experiments (>15 days) may help to improve the uncertainties on $\Delta^{44/40}Ca$ for extremely slow growth rate experiments. Although there are large apparent offsets in the measured fractionation factors from the average value of $\Delta^{44/40}Ca_{s\text{-}f} = -0.08 \pm 0.21$‰ (1σ; Fig. 8), we believe this is an artifact of the large propagated uncertainties on the individual experiments and does not reflect real variability in the fractionation factor.

4. DISCUSSION

4.1. Mineralogy and nanoscale surface structure support non-classical growth

Both FT-IR and XRD observations confirm the formation of non-stoichiometric apatites and/or OCP on the seeded HAP (Table 1 and Figs. 3 and 4). Although the main IR peaks at 560 and 602 cm^{-1} are typical of crystalline HAP (Gadaleta et al., 1996; Berzina-Cimdina and Borodajenko, 2012; Drouet, 2013), attachment of clusters with lower crystallinity leads to broader IR bands. For instance, enlarged OH^- bands between 3600 and 3200 cm^{-1} for the final solids are caused by particle attachment of multi-ion complexes (De Yoreo et al., 2015), forming low crystallinity clusters associated with water molecules (Drouet, 2013). As peaks of phosphate

Table 2
Ca isotope composition ($\delta^{44/40}$Ca) of reactive fluid and solids.

Experiment	Sample type	Time (h)	Ca concentration (mM)[a]	$\delta^{44/40}$Ca (‰)	±2σ err. (‰)	Number of analyses
CaP-1	Fluid	0	1.86	0.1	0.42	2
	Fluid	13	1.82	0.6	0.23	2
	Fluid	78	1.82	0.12	–	1
	Fluid	318	1.81	−0.01	–	1
	Solid	–	–	0.07	0.18	2
CaP-2	Fluid	0	0.98	0.28	0.19	4
	Fluid	8	0.98	0.30	–	1
	Fluid	24	0.98	0.27	0.28	3
	Fluid	266	0.93	0.17	0.16	1
	Solid	–	–	0.34	0.30	2
CaP-3	Fluid	0	1.2	0.21		
	Fluid	9	1.16	0.28	0.01	2
	Fluid	220	1.13	0.30	0.14	3
	Solid	–	–	0.36	0.18	3
CaP-4	Fluid	0	4.49	0.33	–	1
	Fluid	24	4.08	0.28	–	1
	Solid	–	–	0.17	0.04	2
CaP-5	Fluid	0	3.68	0.19	–	1
	Fluid	24	3.26	0.60	–	1
	Solid	–	–	0.33	0.34	4
CaP-6	Fluid	0	2.96	0.44	–	
	Fluid	0.7	2.31	0.27	–	1
	Fluid	9.1	2.12	0.41	0.24	4
	Fluid	52	2.02	0.14	–	1
	Fluid	244	1.99	0.45	0.19	3
	Solid	–	–	0.11	0.09	3
CaP-7	Fluid	0	2.86	0.26	–	1
	Fluid	9	2.32	0.32	–	1
	Fluid	378	2.32	0.23	0.14	4
	Solid	–	–	0.28	–	1
CaP-8	Fluid	0	2.93	0.26	0.04	2
	Fluid	9	2.48	0.52	–	
	Fluid	311	2.47	0.38	0.1	2
	Solid	–	–	0.14	0.16	3
Seed material	Solid	–	–	0.23	0.22	4
SRM 915a	–	–	–	−1.00	0.18	21

[a] Derived from double-spike Ca isotope.

species change with varying pH (Gadaleta et al., 1996; Fig. 2), absorbance at 1020 and 1038, 1112 and 1127 cm^{-1} can be identified as PO_4^{3-} in non-stoichiometric apatite (OCP or brushite) while peaks at 960, 1030, 1055, 1075, 1096 and 1116 cm^{-1} are characteristic peaks of stoichiometric HAP. For the final solids, we observe more pronounced absorbance bands at 1112 and 1020 cm^{-1} than for the seeded HAP suggesting the formation of non-stoichiometric HAP or OCP with preferential attachment of structural non-apatitic PO_4^{3-} (Gadaleta et al., 1996). The formation of brushite or amorphous Ca-phosphates (ACP) can be ruled out based on X-ray diffraction data. Brushite typically exhibits diffraction peaks at 11.6° and 20.6° (RRUFF R070554) and the formation of ACP is characterized by a diffusive broad peak between 27° and 37° (Posner and Betts, 1975; Sauer and Wuthier, 1988; Gadaleta et al., 1996; Dorozhkin, 2009; Jiang et al., 2017). Thus, we conclude that the precipitates are Ca-deficient and are most likely formed of non-stoichiometric HAP or OCP rather than other Ca-phosphates such as brushite or ACP.

The results of this study show that pH strongly influences growth kinetics and whether HAP growth proceeds by a precursor-mediated pathway. As the studied pH values for all experiments were above pH 6.5, the predominant phases are OCP and HAP. This is agreement with previous observations that the formation of HAP is either preceded by OCP (pH < 6.9; Nancollas and Koutsoukos, 1980; Van Kemenade and Bruyn, 1987; Wang and Nancollas, 2008) or dominated by the formation of Ca-deficient HAP at pH ~ 7 (Fulmer, 1992). Based on the steady-state pH (~4 h), we also assume that the aqueous solutions have also reached

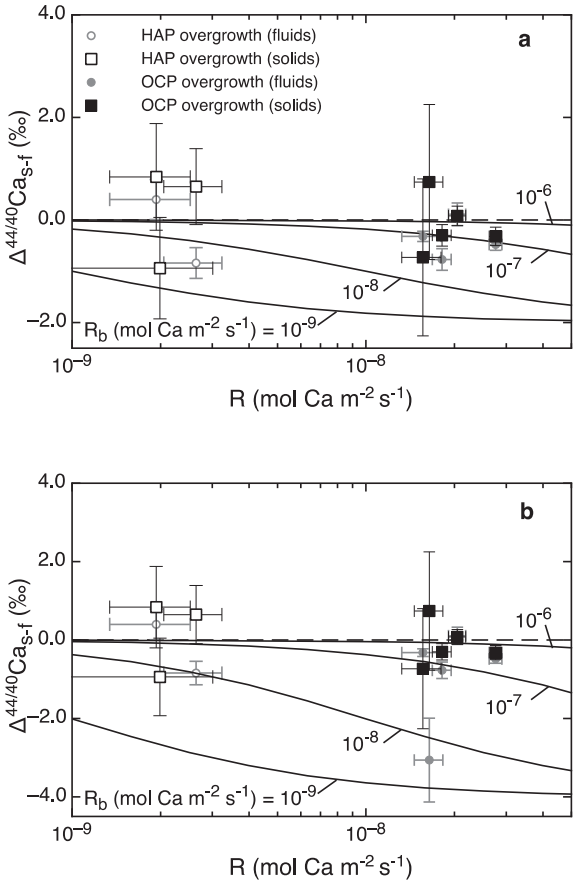

Fig. 8. Measured Ca isotope fractionation ($\Delta^{44/40}Ca_{s\text{-}f}$) as a function of growth rate (mol Ca m^{-2} s^{-1}) compared with model curves representing classical crystal growth. Measured values are derived from the measured $\delta^{44/40}$Ca of the fluids (circles) and final solids (squares) listed in Table 2. Filled symbols represent $\Delta^{44/40}Ca_{s\text{-}f}$ data for experiments with predominantly OCP overgrowth, while open symbols represent HAP overgrowth. Model curves are calculated assuming various back reaction rates and kinetic endmember fractionation factors $\alpha_f = 0.998$ (A) and 0.996 (B). Error bars are propagated based on the uncertainties of the measured fluid Ca concentrations (±1%) and $\delta^{44/40}$Ca values (±0.1‰, 1σ).

chemical equilibrium in terms of aqueous calcium and orthophosphate speciation.

The co-occurrence of OCP and HAP phases is ubiquitous during synthetic growth of Ca-phosphates due to the structural similarity between HAP and OCP, which consists of alternating domains of HAP and of structural water (Zhan et al., 2005; Pompe et al., 2015). As a result, these phases can form lamellar mixtures and easily undergo epitaxial growth (Brown et al., 1962; Fernandez et al., 2003). Stoichiometric HAP has an atomic Ca/P ratio of 1.67 with 39% (weight) of Ca, 18.5% P and 3.38% of OH, but is often Ca-depleted (cf. Fulmer et al., 1992), while pure OCP has a lower Ca/P ratio of 1.33. The precipitation of HAP has long been thought to involve formation of a precursor phase, usually OCP (Wang and Nancollas, 2008; Onuma and Sugiura, 2015; Pompe et al., 2015; Li et al., 2016a), although amorphous Ca-phosphate (ACP; Habraken

Table 3
Growth rates (R mol Ca m^2 s^{-1}) and their errors and calculated Ca fractionation factors Δ ($\Delta^{44/40}$Ca) and $\Delta^{44/40}$Ca errors. The $\Delta^{44/40}Ca_{s\text{-}f}$ (solid) are calculated on differences in $\delta^{44/40}$Ca between the solid and aqueous solution during growth. The $\Delta^{44/40}$Ca values (fluid) are based on the differences in the aqueous $\delta^{44/40}$Ca of the influent and effluent solutions.

Exp.	Ca phosphate	R (mol Ca m^{-2} s^{-1})	Err R (mol Ca m^{-2} s^{-1})	Fraction overgrowth (%)	$\Delta^{44/40}Ca_{s\text{-}f}$ (solid)	±1σ err. $\Delta^{44/40}Ca_{s\text{-}f}$ (solid)	$\Delta^{44/40}$Ca (fluid)	±1σ err. $\Delta^{44/40}$Ca (fluid)
CaP-1	HAP	1.99×10^{-9}	1.02×10^{-9}	14.3	−0.94	0.99	nd	nd
CaP-2	HAP	1.93×10^{-9}	5.92×10^{-10}	13.0	0.84	1.0	0.40	0.39
CaP-3	HAP	2.64×10^{-9}	5.90×10^{-10}	18.1	0.65	0.74	−0.84	0.30
CaP-4	OCP	1.56×10^{-8}	2.38×10^{-9}	8.9	−0.73	1.5	−0.32	0.10
CaP-5	OCP	1.64×10^{-8}	1.83×10^{-9}	9.1	0.74	1.5	−3.1	1.1
CaP-6	OCP	2.76×10^{-8}	1.37×10^{-9}	68.2	−0.32	0.18	−0.48	0.11
CaP-7	OCP	2.05×10^{-8}	1.38×10^{-9}	64.7	0.08	0.19	0.11	0.22
CaP-8	OCP	1.82×10^{-8}	1.34×10^{-9}	60.3	−0.30	0.21	−0.77	0.21

et al., 2013), brushite (Barone et al. 1976; Wang and Nancollas, 2008), and tricalcium phosphate (TCP, $Ca_3(PO_4)_2$) precursors have also been observed. Subsequent transformation from OCP to thermodynamically favorable HAP can occur by solid-state hydrolysis with loss of phosphate (Brown et al., 1962; Zhan et al., 2005; Pompe et al., 2015), meaning recrystallization need not reset the Ca isotopic composition of the solid phase.

Observed structural features on the final solids using AFM imaging provide strong evidence that polynuclear growth is the dominant growth mechanism over a wide range of supersaturations (Fig. 6). Our observations are consistent with prior in-situ AFM growth experiments for HAP (Onuma, 1995, 1996; Li et al., 2016a), indicating cluster attachment to the seed material. Pre-existing particles of 1–2 nm heights at the {1 0 0} face of the initial seeded HAP (Fig. 6a) are identical to the surface morphology observations by Li et al. (2016a). These features are similar in size to Posner's clusters (0.95 nm; Posner and Betts, 1975; Kanzaki et al., 2001), which have been proposed as stable growth units for the non-classical growth mechanism (Kanzaki et al., 2001; Gebauer and Cölfen, 2011; Wang et al., 2012; Habraken et al., 2013).

Regardless of the mineralogy of the overgrowth material, precipitation is dominated by cluster deposition on the seeded HAP. In experiments CaP-4 and -8, step-like features are apparent, but step heights are greater than the molecular unit width of PO_4^{3-} (Fig. 6e–h), also suggesting cluster attachment (Onuma et al., 1995, 1996). In experiments CaP-2 and -3, which were undersaturated with respect to OCP, the surface growth features indicate that direct cluster deposition on terraces is the dominant growth pathway (Fig. 6c–d). Although in-situ AFM images of HAP growth have captured features of classical spiral growth during short-duration experiments, this mechanism was not thought to contribute significantly to the overall growth (Li et al., 2016a). We find no evidence of spiral growth from our ex-situ AFM images, possibly because any spiral growth features have been superimposed by nano-cluster attachment over the duration of the experiments (24 h or 15 days). Moreover, the presence of spiral or step growth features is not sufficient to rule out a non-classical growth pathway, as the very low step kinetic coefficients observed on HAP are consistent with attachment of clusters and not monomer ions along the step (Onuma and Ito, 1998).

4.2. Ca isotope data support non-classical (polynuclear) growth

The surface area normalized Ca-phosphate growth rates calculated assuming constant specific surface area exhibit slower growth rates for HAP than for OCP formation relative to the solution supersaturation. The observation of faster growth rates and OCP formation occurring at lower pH is consistent with previous studies (cf. Wang and Nancollas, 2008). However, these surface area normalized growth rates represent maximum values, because it is likely that the surface area increased throughout the experiment as seen in the SEM images (Fig. 2). As we also did not precipitate sufficient material over the course of the experiments, we were not able to quantify changes in surface area using the BET method. However, material precipitated under similar growth conditions, albeit with a much higher surface area seed material (35 m^2/g) were found to have final specific surface areas ranging from 23 to 28 m^2/g (Christoffersen and Christoffersen, 1992). Thus, at a maximum, we estimate these surface area normalized rates to be 42-fold too high. The rates of non-classical growth processes should be largely independent of the surface area of the seed material, because growth is controlled by nucleation and aggregation phenomena, and thus our calculated growth rates should reflect qualitative trends.

The absence of a kinetic isotope effect as evidenced by the aggregate Ca isotope data supports the hypothesis that the growth of Ca-phosphates (HAP and OCP) is controlled by a non-classical growth mechanism, involving attachment and deposition of nano-clusters, whose formation dynamics are likely controlled by ion and cluster transport and not surface reaction. During surface-reaction controlled growth of Ca-phosphates and other Ca-mineral phases, the precipitation rate is expected to be controlled by the dynamics of Ca desolvation at active growth sites on the mineral surface (cf. Christoffersen et al., 1996; Casey and Rustad, 2007; Hofmann et al., 2012; Colla et al., 2013; Harouaka et al., 2017). If the attachment of single Ca^{2+} ions is growth rate-limiting, the lighter isotope of Ca is expected to be preferentially incorporated in the Ca-phosphates causing the $\Delta^{44/40}Ca$ to vary systematically with supersaturation, as observed for ion-by-ion growth of calcite (DePaolo et al., 2011). The magnitude of kinetic isotope fractionation arising from Ca desolvation during surface reaction can be estimated based on a limited number of variables: net precipitation rate (R_p), reverse reaction rate (R_b), and kinetic and equilibrium end-member fractionation factors (α_f and α_{eq}; DePaolo et al., 2011).

Making reasonable assumptions about the end-member fractionation factors for Ca derived from calcite growth experiments and molecular simulations ($\alpha_f = 0.996$ or 0.998 and $\alpha_{eq} = 1.000$; DePaolo et al., 2011; Hofmann et al., 2012; Nielsen et al, 2012), we determined the expected Ca isotope fractionation factor as a function of growth rate for a wide range of back reaction rates (Fig. 8a–b). We find that we must assume an unreasonably high value of R_b at pH 7 (*i.e.*, $R_b > 10^{-6.4}$ mol Ca m^{-2} s^{-1} for $\alpha_f = 0.996$ and $R_b > 10^{-6.7}$ mol Ca m^{-2} s^{-1} for α_f =0.998) to a fractionation factor that is sufficiently small to explain the results of the fast growth rate experiment CaP-6 ($\Delta^{44/40}Ca_{s\text{-}f} = -0.32 \pm 0.18‰$; $R_p = 2.8 \times 10^{-8}$ mol Ca m^{-2} s^{-1}). Even if we assume a much higher specific surface area of 28 m^2/g for this experiment, the required R_b has to be either greater than 10^{-8} mol Ca m^{-2} s^{-1} for α_f of 0.996 (*i.e.*, $\Delta^{44/40}Ca_{s\text{-}f} = -4.0‰$) or greater than $10^{-8.3}$ mol Ca m^{-2} s^{-1} for α_f of 0.998 (*i.e.*, $\Delta^{44/40}Ca_{s\text{-}f} = -2.0‰$), respectively. The maximum feasible value for R_b can be determined by the dissolution rate of the mineral at infinite undersaturation at the pH of interest (DePaolo, 2011). A reasonable estimate for the maximum HAP dissolution rates at circumneutral pH is two orders of magnitude lower than required 2.3×10^{-10} mol Ca m^{-2} s^{-1} (Valsami-Jones et al., 1998; pH

6.7). To our knowledge there are no OCP dissolution rates available in the relevant pH range, but even at lower pH, OCP dissolution is only a factor of ~1.2 greater than that of HAP (Wang and Nancollas, 2008). We conclude that the measured Ca isotope data are inconsistent with a classical growth process in which dissociative desolvation of Ca ions at the surface are the rate-limiting mechanism.

The foregoing analysis relies on the assumption that the kinetic end-member fractionation factor associated with Ca ion attachment to the growth surface is similar to the value obtained from the calcite kinetic Ca isotope effect (DePaolo, 2011; Nielsen et al., 2012), or from bulk aqueous solution (Hofmann et al., 2012), and that Ca ion desolvation is rate limiting during classical HAP growth. If instead another process such as hydrolysis controls the rate of classical HAP growth (cf. Christoffersen et al., 1998b), the Ca isotope composition of HAP could be controlled by other factors, such as face-specific equilibrium fractionation (Haraouka et al., 2017), equilibrium aqueous speciation (Colla et al., 2018), or molecular diffusion-controlled fractionation (Bourg et al., 2010) under transport-limited growth conditions. In the case of experiments involving an OCP precursor, a rate limitation by hydrolysis can be ruled out, because OH^- is not a stoichiometric constituent of OCP. Subsequent abiogenic conversion of OCP to HAP requires hydrolysis but is not thought to involve a dissolution-reprecipitation step that would reset the Ca isotope composition (Zhan et al., 2005). Thus, we conclude that the absence of a clear kinetic isotope effect is consistent with nanostructural and mineralogical evidence for the non-classical growth of Ca-phosphates over a wide range of supersaturations and growth rates at circumneutral pH. This process results in particle attachment where stochastic collision of Ca and phosphate ions in the bulk solution lead to the spontaneous formation of nanoclusters or multi-ion complexes, which subsequently aggregate (Gebauer and Cölfen, 2011; Habraken et al., 2013).

4.3. Geological and biological implications

Our results suggest that at circum-neutral pH and ambient temperatures, Ca isotope fractionation between synthetic Ca-phosphates and solution is independent of precipitation rate and is within error of 0‰, although the large magnitude of experimental uncertainties, especially at the slowest growth rates, may mask a kinetic isotope effect. Below we discuss the implications of this conclusion in the context of apatite formation in geological and biological systems, specifically the mechanisms governing authigenic phosphate formation and biocalcification and corresponding their Ca isotopic signatures.

4.3.1. Ca phosphates in marine environments

The interpretation of our experimental data implies that the Ca isotopic signatures of inorganically formed Ca-phosphates (*i.e.,* authigenic apatite) may directly reflect the fluid composition from which the crystals are originated. As polynuclear growth for OCP seems not induce significant Ca isotope fractionation at circum-neutral pH, the Ca isotopic signature of the fluid is preserved in the solid phase. The two main caveats to this conclusion are the very large uncertainties on some of the experimental Ca fractionation factors, and the fact that the growth solutions do not mimic the composition of seawater. The primary difference between our laboratory experiments and the growth conditions for HAP and OCP in marine sediments is that experimental growth solutions were composed to precipitate only pure Ca-phosphates omitting elements present in seawater (*i.e.,* Mg^{2+}, Cl^-, F^-), which can be incorporated in the crystal lattice and lower growth rates or even inhibit the formation of Ca-phosphates (Salimi et al., 1985; Van Cappellen and Berner, 1989; Gunnars et al., 2004). Nevertheless, our data demonstrate that the $\delta^{44/40}$Ca of precursor OCP may capture the marine porewater Ca isotopic composition, because OCP formation is a kinetic barrier to apatite precipitation in marine systems (Gunnars et al., 2004). It has been shown that there is no apatite precipitation until marine porewater is supersaturated with respect to OCP, even if the solution is supersaturated with respect to HAP (Gunnars et al., 2004).

Unlike our synthetic Ca-phosphates, earlier studies indicate that authigenic marine phosphate peloids are approximately 1‰ lighter in $\delta^{44/40}$Ca than modern seawater, with less than a 1‰ range in values attributed to changes in the $\delta^{44/40}$Ca seawater composition over time (Schmitt et al., 2003; Soudry et al., 2004). The fact that these authigenic Ca phosphate minerals are isotopically light relative to seawater is at first glance in conflict with our experimental findings. However, it is likely that this difference is attributable to the fact that the Ca isotope composition of pore water is isotopically light compared to seawater due to equilibration with calcium carbonate minerals (cf. Fantle and DePaolo, 2007). The precipitation from pore fluid of authigenic Ca-phosphate peloids, which form during early diagenesis (Riggs et al., 1997), may preserve the Ca isotope composition of pore water that is isotopically light with respect to seawater. Alternatively, these light isotope compositions could reflect isotope fractionation during the direct formation of an isotopically light Ca-phosphate phase. Marine phosphorites consist mainly of carbonated fluorapatite and hydroxyapatite (Schmitt et al., 2003), and unlike HAP, fluorapatite may precipitate by a classical growth pathway (Liu and Nancollas, 1996). Thus, future studies should be done to ascertain whether synthetic fluorapatite precipitation is associated with Ca isotope fractionation and enrichment of ^{40}Ca in the solid phase. Taken together, Ca isotope ratios can provide an additional constraint on pore fluid and (potentially) seawater chemistry and may help to reconstruct the marine cycle P through geologic history.

4.3.2. Biogenic apatite in biological and geological systems

The majority of phosphorite formation in marine sedimentary environments is biologically mediated by phosphate release from bacterial cells (Schulz and Schulz, 2005), so a direct conclusion on apatite formation in natural settings should be drawn with some caution. Calcium isotope fractionation is known to occur during biocalcification (Skulan et al., 1997). Thus, differences in Ca isotopic effects between inorganically formed Ca-phosphate in our

study compared to biogenic apatites (Skulan and DePaolo, 1999; Hinojosa et al., 2012; Li et al., 2016b) may be due to either abiogenic growth mechanisms or physiological processes that are not yet well understood. Generally, biomineral HAP typically contains carbonate ion impurities (up to 10% in vertebrate skeletal material), and its formation is characterized by more complex fluid composition including functional organic molecules (Zhan et al., 2005; Wang and Nancollas, 2008). Whether aqueous organic species or other factors associated with microbially mediated growth can affect the Ca isotopic composition of HAP and its precursor phases should be addressed in future studies.

5. CONCLUSION

Our study provides several lines of evidence that polynuclear (cluster) growth is the dominant growth mechanism for HAP and for its precursor phase OCP. Within the tested range of supersaturations, direct nucleation via precursor phases dominates over direct ion incorporation processes, which is supported by both the absence of kinetic Ca isotope fractionation ($\Delta^{44/40}$Ca) and by the polynuclear growth features observed in nanoscale images. The Ca isotopic composition of OCP and possibly HAP could be a good proxy for fluid isotopic signature from which the Ca-phosphates originate, but further work is required to understand the influence of mineralogy, diagenesis, and biologic factors on the Ca isotopic composition of the preserved apatite.

ACKNOWLEDGEMENTS

All authors contributed to the research and manuscript. KS performed the experiments, KS and STB conducted the isotope analyses, KS obtained the AFM images, and LNL completed the calculations. KS and LNL wrote the manuscript with advice and revisions from STB.

The authors gratefully acknowledge support from the University of California Agricultural Experiment Station through the USDA National Institute of Food and Agriculture for the Hatch Project Accession Number 1004013, and from the Director, Office of Science, Office of Basic Energy Sciences, of the U.S. Department of Energy under Contract No. DE-AC02- 05CH11231. We thank Tim Teague and Andy Yang for their assistance with analytical measurements. The authors also thank M.S. Fantle and two anonymous reviewers for their constructive comments and the associate editor Martin Novak for suggestions that have significantly improved this manuscript.

REFERENCES

Amini M., Eisenhauer A., Böhm F., Holmden C., Kreissig K., Hauff F. and Jochum K. P. (2009) Calcium isotopes ($\delta^{44/40}$Ca) in MPI-DING reference glasses, USGS rock powders and various rocks: Evidence for Ca isotope fractionation in terrestrial silicates. *Geostand. Geoanal. Res.* **33**, 231–347.

Arey J. S., Seaman J. C. and Bertsch P. M. (1998) Immobilization of uranium in contaminated sediments by hydroxyapatite. *Environ. Sci. Technol.* **33**, 337–342.

Barone J. P., Nancollas G. H. and Tomson M. (1976) The seeded growth of calcium phosphates. The kinetics of growth of dicalcium phosphates dihydrates on hydroxyapatite. *Calcif. Tiss. Res.* **21**, 171–182.

Berzina-Cimdina L. and Borodajenko N. (2012) Research of calcium phosphates using fourier transform infrared spectroscopy. In *Infrared Spectroscopy- Materials Science, Engineering and Technology*. In Tech. https://doi.org/10.5772/2055.

Bourg I. C., Richter F. M., Christensen J. N. and Sposito G. (2010) Isotopic mass dependence of metal cation diffusion coefficients in liquid water. *Geochim. Cosmochim. Acta* **74**(8), 2249–2256.

Brown W. E., Smith J. P., Lehr J. R. and Frazier A. W. (1962) Octacalcium phosphate and hydroxyapatite: crystallographic and chemical relations between octacalcium phosphate and hydroxyapatite. *Nature* **196**, 1050–1055.

Burton W. K., Cabrera N. and Frank F. C. (1951) The growth of crystals and the equilibrium structure of their surfaces. *Phil. Trans. A* **243**, 299–358.

Casey W. H. and Rustad J. R. (2007) Reaction dynamics, molecular clusters, and aqueous geochemistry. *Annu. Rev. Earth Planet. Sci.* **35**, 21–46.

Christoffersen M. R. and Christoffersen J. (1992) Possible mechanisms for the growth of the biomaterial, calcium hydroxyapatite microcrystal. *J. Cryst. Growth* **121**, 617–630.

Christoffersen J., Christoffersen M. R. and Johansen T. (1996) Some new aspects of surface nucleation applied to the growth and dissolution of fluroapatite and hydroxyapatite. *J. Cryst. Growth* **163**, 304–310.

Christoffersen M. R., Dohrup J. and Christoffersen J. (1998a) Kinetics of growth and dissolution of calcium hydroxyapatite in suspensions with variable calcium to phosphate ratio. *J. Cryst. Growth* **186**, 283–290.

Christoffersen M. R., Dohrup J. and Christoffersen J. (1998b) The importance of formation of hydroxyl ions by dissociation of trapped water molecules for growth of calcium hydroxyapatite crystals. *J. Cryst. Growth* **186**, 275–282.

Colla C. A., Wimpenny J., Yin Q. Z., Rustad J. R. and Casey W. H. (2013) Calcium-Isotope Fractionation Between Solution and Solids with Six, Seven or Eight Oxygens Bound to Ca(II). *Geochim. Cosmochim. Acta* **121**, 363–373.

Colla C. A., Casey W. H. and Ohlin C. A. (2018) Computational Prediction of Mg-Isotope Fractionation Between Aqueous $[Mg(OH2)_6]^{2+}$ and Brucite. *Geochim. Cosmochim. Acta* **227**, 64–74.

Conca J. L. and Wright J. (2006) An apatite II permeable reactive barrier to remediate groundwater containing Zn, Pb, and Cd. *Appl. Geochem.* **21**, 2188–2200.

Conley D. J., Paerl H. W., Howarth R. W., Boesch D. F., Seitzinger S. P., Havens K. E., Lancelot C. and Likens G. E. (2009) Controlling eutrophication: Nitrogen and phosphorous. *Science* **323**, 1014–1015.

Daniel T. C., Sharpley A. N. and Lemunyon J. L. (1998) Agricultural phosphorous and eutrophication: A symposium overview. *J. Environ. Qual.* **27**, 251–257.

DePaolo D. J. (2011) Surface kinetic model and trace element fractionation during precipitation of calcite from aqueous solutions. *Geochim. Cosmochim. Acta* **75**, 1039–1056.

DePaolo D. J. (2004) Calcium isotopic variations produced by biological, kinetic, radiogenic and nucleosynthetic processes. *Rev. Mineral. Geochem.* **55**.

De Yoreo J. J., Gilbert P. U. P. A., Sommerdijk N. A. J. M., Penn R. L., Whitelam S., Joester D., Zhang H., Rimer J. D., Navrotsky A., Banfield J. F., Wallace A. F., Michel F. M., Meldrum F. C., Cölfen H. and Dove P. M. (2015) Crystallization by particle attachment in synthetic, biogenic, and geological environments. *Science* **349**, 498–507.

Dorozhkin S. V. (2009) Nanodimensional and nanocrystalline apatites and other calcium orthophosphates in biomedical engineering, biology and medicine. *Materials* **2**, 1975–2045.

Drouet C. (2013) Apatite formation: why it may not work as planned, and how to conclusively identify apatite compounds. *BioMed Res. Intern.* **2013**, 12. Article ID 490946.

Elser J. J., Bracken M. E. S., Cleland E. E., Gruner D. S., Harpole W. S., Hillebrand H., Ngai J. T., Seabloom E. W., Shurin J. B. and Smith J. E. (2007) Global analysis of nitrogen and phosphorous limitation of primary producers in freshwater, marine and terrestrial ecosystems. *Ecol. Lett.* **10**, 1135–1142.

Elser J. J. and Bennett E. (2011) Phosphorous cycle: A broken biogeochemical cycle. *Nature* **478**, 29–31.

Fantle M. S. and DePaolo D. J. (2007) Ca isotopes in carbonates sediments and pore fluid from ODP Site 807A: The Ca2+ (aq)-calcite equilibrium fractionation factor and calcite recrystallization rates in Pleistocene sediments. *Geochim. Cosmochim. Acta* **71**, 2524–2546.

Fernandez E., Gil F., Ginebra M., Driessens F., Planell J. and Best S. (1999) Calcium phosphate bone cements for clinical applications. Part I: solution chemistry. *J. Mater. Sci. Mater. Med.* **10**(3), 169–176.

Fernandez M. E., Zorrilla-Cangas C., Garcia-Garcia R., Ascencio J. A. and Reyes-Gasga J. (2003) New model for the hydroxyapatite-octacalcium phosphate interface. *Acta Cryst. B* **59**, 175–181.

Filippelli G. M. (2008) The global phosphorous cycle: Past, present, and future. *Elements* **4**, 89–95.

Filippelli G. M. (2011) Phosphate rock formation and marine phosphorus geochemistry: the deep time perspective. *Chemosphere* **84**, 759–766.

Fulmer M. T., Martin R. I. and Brown P. W. (1992) Formation of calcium deficient hydroxyapatite at near-physiological temperature. *J. Mater. Sci.* **4**, 299–305.

Gadaleta S. J., Paschalis E. P., Betts F., Mendelsohn R. and Boskey A. L. (1996) Fourier transform infrared spectroscopy of the solution-mediated conversion of amorphous calcium phosphate to hydroxyapatite: New correlations between X-ray diffraction and infrared data. *Calc. Tiss. Int.* **58**, 9–16.

Gebauer D. and Cölfen H. (2011) Prenucleation clusters and non-classical nucleation. *Nanotoday* **6**, 564–584.

Guidry M. W. and Mackenzie F. T. (2000) Apatite weathering and the Phanerozoic phosphorous cycle. *Geology* **28**, 631–634.

Guidry M. W. and MacKenzie F. T. (2003) Experimental study of igneous and sedimentary apatite dissolution: Control of pH, distance from equilibrium, and temperature on dissolution rates. *Geochim. Cosmochim. Acta* **67**, 2949–2963.

Gunnars A., Blomqvist S. and Martinsson C. (2004) Inorganic formation of apatite in brackish seawater from Baltic Sea: an experimental approach. *Mar. Chem.* **91**, 15–26.

Gussone N., Eisenhauer A., Heuser A., Dietzel M., Bock B., Boehm F., Spero H. J., Lea D. W., Bijma J. and Naegler T. F. (2003) Model for kinetic effects on calcium isotope fractionation (δ^{44}Ca) in inorganic aragonite and cultured planktonic foraminifera. *Geochim. Cosmochim. Acta* **667**, 1375–1382.

Habraken W. J. E. M., Tao J., Brylka L. J., Friedrich H., Bertinetti L., Schenk A. S., Verch A., Dmitrovic V., Bomans P. H. H., Frederik P. M., Laven J., van der Schoot P., Aichmayer B., de With G., De Yoreo J. J. and Sommerdijk N. A. J. M. (2013) Ion-association complexes unite classical and non-classical theories for the biomimetic nucleation of calcium phosphate. *Nature Commun.* **4**, 1507.

Harouaka K., Kubicki J. D. and Fantle M. S. (2017) Effect of amino acids on the precipitation kinetics and Ca isotopic composition of gypsum. *Geochim. Cosmochim. Acta* **218**, 343–364.

Hinojosa J. L., Brown S. T., Chen J., DePaolo D. J., Paytan A., Shen S.-Z. and Payne J. L. (2012) Evidence for end-Permian ocean acidification from calcium isotopes in biogenic apatite. *Geology* **40**, 743–746.

Hofmann A. E., Bourg I. C. and DePaolo D. J. (2012) Ion desolvation as a mechanism for kinetic isotope fractionation in aqueous systems. *PNAS* **109**, 18689–18694.

Holmden C., Papanastassiou D. A. and Blanchon P. (2012) $\delta^{44/40}$Ca variability in shallow water carbonates and the impact of submarine groundwater discharge on Ca-cycling in marine environments. *Geochim. Cosmochim. Acta* **83**, 179–194.

Horwitz E. P., McAlister D. R., Bond A. H. and Barrans R. E. (2005) Novel extraction of chromatographic resins based on tetraalkyldiglycolamides: Characterization and potential applications. *Solvent Extr. Ion Exch.* **23**, 319–344.

House W. A. (1999) The physico-chemical conditions for the precipitation of phosphate with calcium. *Environ. Technol.* **20**, 727–733.

Hughes J. M. and Rakovan J. F. (2015) Structurally robust, chemically diverse: Apatite and apatite supergroup minerals. *Elements* **11**.

Jahnke R. A., Emerson S. R., Roe K. K. and Burnett W. C. (1983) The present day formation of apatite in Mexican continental margin sediments. *Geochim. Cosmochim. Acta* **47**, 259–266.

Jiang S., Jin W., Wang Y.-N., Pan H., Sun Z. and Tang R. (2017) Effect of the aggregation state of amorphous calcium phosphates on hydroxyapatite nucleation kinetics. *RSC Adv.* **7**, 25497.

Johnsson M. S. A. and Nancollas G. H. (1992) The role of brushite and octacalcium phosphates in apatite formation. *Crit. Rev. Oral Biol. Med.* **3**.

Kanzaki N., Treboux G., Onuma K., Tsutsumi S. and Ito A. (2001) Calcium phosphate clusters. *Biomaterials* **22**, 2921–2929.

Koutsopoulos S. (2002) Synthesis and characterization of hydroxyapaptite crystals: A review study on the analytical methods. *J. Biomed. Mater. Res.* **62**, 600–612.

Koutsoukos P. G. (1998) Growth of calcium phosphates on different substrates: Epitaxial considerations. In *IN Calcium Phosphates in Biological and Industrial Systems*. Springer US, pp. 41–66.

Lammers L. N., Rasmussen H., Adilman D., deLemos J. L., Zeeb P., Larson D. G. and Quicksall A. N. (2017) Groundwater uranium stabilization by a metastable hydroxyapatite. *Appl. Geochem.* **84**, 105–113.

Lemarchand D., Wasserburg G. J. and Papanastassiou D. A. (2004) Rate-controlled calcium isotope fractionation in synthetic calcite. *Geochim. Cosmochim. Acta* **68**, 4665–4678.

Li M., Wang L., Zhang W., Putnis C. V. and Putnis A. (2016a) Direct observation of spiral growth, particle attachment, and morphology evolution of hydroxyapatite. *Cryst. Growth Des.* **8**, 4509–4518.

Li Q., Thirlwall M. and Muller W. (2016b) Ca isotopic analysis of laser-cut microsamples of (bio)apatite without chemical purification. *Chem. Geol.* **422**, 1–12.

Liu Y. and Nancollas G. H. (1996) Fluorapatite growth kinetics and the influence of solution composition. *J. Cryst. Growth* **165**, 116–123.

Nancollas G. H. and Koutsoukos P. (1980) Calcium phosphate nucleation and growth in solution. *Prog. Cryst. Growth Charact.* **3**, 77–102.

Niederberger M. and Cölfen H. (2006) Oriented attachement and mesocrystals: Non-classical crystallization mechanisms based on nanoparticle assembly. *Phys. Chem. Chem. Phys.* **8**, 3271–3287.

Nielsen L. C., DePaolo D. J. and De Yoreo J. J. (2012) Self-consistent ion-by-ion growth moel for kinetic isotopic fractionation during calcite precipitation. *Geochim. Cosmochim. Acta* **86**, 166–181.

Onuma K., Ito A., Tateishi T. and Kameyama T. (1995) Growth kinetics of hydroxypapatite crystal revealed by atomic force microscopy. *J. Cryst. Growth* **154**, 118–125.

Onuma K., Ito A. and Tateishi T. (1996) Investigation of a growth unit hydroxyapatite crystal from the measurements of step kinetics. *J. Cryst. Growth* **167**, 773–776.

Onuma K. and Ito A. (1998) Cluster growth model for hydroxyapatite. *Chem. Mater.* **11**, 3346–3351.

Onuma K. (2006) Recent research on pseudobiological hydroxyapatite crystal growth and phase transition mechanisms. *Prog. Cryst. Growth Charact. Mater.* **52**, 223–245.

Onuma K. and Sugiura Y. (2015) Metastable intermediate phase during the phase transformation of calcium phosphates. *J. Biotechnol. Biomater.* **5**, 214–217.

Oxmann J. F. and Schwendenmann L. (2014) Quantification of octacalcium phosphate, authigenic apatite and detrital apatite in coastal sediments using differential dissolution and standard addition. *Ocean Sci.* **10**, 571–585.

Palmer L. C., Newcomb C. J., Kaltz S. R., Spoerke E. D. and Stupp S. I. (2008) Biomimetic systems for hydroxyapatite mineralization inspired by bone and enamel. *Chem. Rev.* **108**, 4754–4783.

Pompe W., Worch H., Habraken W. J. E. M., Simon P., Kniep R., Ehrlich H. and Paufler P. (2015) Octacalcium phosphate - a metastable mineral phase controls the evolution of scaffold forming proteins. *J. Mater. Chem. B* **3**, 5318–5329.

Posner A. S. and Betts F. (1975) Synthetic amorphous calcium phosphates and its relation to bone mineral structure. *Acc. Chem. Res.* **8**, 273–281.

Rietveld H. M. (1969) A profile refinement method for nuclear and magnetic structures. *J. Appl. Cryst.* **2**, 65–71.

Riggs S., Stille P. and Ames D. (1997) Sr isotopic age analysis of co-occurring Miocene phosphate grain types on the North Carolina continental shelf. *J. Sediment. Res.* **67**, 65–73.

Rokidi S., Combes C. and Koutsoukos P. G. (2011) The calcium phosphate- calcium carbonate system: growth of octacalcium phosphate in calcium carbonates. *Cryst. Growth Des.* **11**, 1683–1688.

Ruttenberg K. C. and Berner R. A. (1993) Authigenic apatite formation and burial in sediments from non-upwelling, continental margin environments. *Geochim. Cosmochim. Acta* **57**, 991–1007.

Ruttenberg K. C. (2003) The global phosphorous cycle. In *Treatise on Geochemistry*, vol. 8. (ed. W. H. Schlesinger). Elsevier, pp. 585–643.

Salimi M. H., Heughebaert J. C. and Nancollas G. H. (1985) Crystal growth of calcium phosphates in the presence of magnesium ions. *Langmuir* **1**, 119–122.

Sauer G. R. and Wuthier R. E. (1988) Fourier transform infrared characterization of mineral phases formed during induction of mineralization by collagenase-released matrix vesicles in vitro. *J. Biol. Chem.* **263**, 13718–13724.

Schmitt A.-D., Stille P. and Vennemann T. (2003) Variations of the 44/40Ca ratio in seawater during the past 24 million years: Evidence from δ^{44}Ca and δ^{18}O values of Miocene phosphates. *Geochim. Cosmochim. Acta* **67**, 2607–2614.

Schulz H. N. and Schulz H. D. (2005) Large sulfur bacteria and the formation of phosphorite. *Science* **307**, 5708.

Seaman J. C., Arey J. S. and Bertsch P. M. (2001) Immobilization of nickel and other metals in contaminated sediments by hydroxyapatite addition. *J. Environ. Qual.* **30**, 460–469.

Simon F. G., Biermann V. and Peplinski B. (2008) Uranium removal from groundwater using hydroxyapatite. *Appl. Geochem.* **23**, 2137–2145.

Skulan J., DePaolo D. J. and Owens T. L. (1997) Biological control of calcium isotopic abundances in the global calcium cycle. *Geochim. Cosmochim. Acta* **61**, 2505–2510.

Skulan J. and DePaolo D. J. (1999) Calcium isotope fractionation between soft and mineralized tissues as a monitor of calcium use in vertebrates. *PNAS* **96**, 13709–13713.

Soudry D., Segal I., Nathan Y., Glenn C. R., Halicz L., Lewy Z. and VonderHaar D. L. (2004) 44/42Ca and 143Nd/144Nd isootpe variations in Cretaceous-Eocene Tethyan francolites and their bearing on phsphogenesis in the southern Tethys. *Geology* **32**, 389–392.

Tang J., Dietzel M., Boehm F., Koehler S. J. and Eisenhauer A. (2008) Sr2+/Ca2+ and 44Ca/40Ca fractionation during inorganic calcite formation: IICa isotopes. *Geochim. Cosmochim. Acta* **72**, 3733–3745.

Tas A. C. (2001) Molten salt synthesis of calcium hydroxyapatite whiskers. *J. Am. Ceram. Soc.* **84**, 295–300.

Tyrell T. (1999) The relative influences of nitrogen and phosphorous on oceanic primary production. *Nature* **400**, 525–531.

Valsami-Jones E., Ragnarsdottir K. V., Putnis A., Bosbach D., Kemp A. J. and Cressey G. (1998) The dissolution of apatite in the presence of aqueous metal cations at pH 2–7. *Chem. Geol.* **151**, 215–233.

Van Cappellen P. and Berner R. A. (1989) Crystal growth of marine apatite. *Chem. Geol.* **84**, 331–333.

Van Kemenade M. J. J. M. and de Bruyn P. L. (1987) A kinetic study of precipitation from supersaturated calcium phosphate solutions. *J. Colloid Interface Sci.* **118**, 564–585.

Wang L., Li S., Ruiz-Agudo E., Putnis C. V. and Putnis A. (2012) Posner's cluster revisited: Direct imaging of nucleation and growth of nanoscale calcium phosphate clusters at the calcite-water interface. *Cryst. Eng. Comm.* **14**, 6252–6256.

Wang L. and Nancollas G. H. (2008) Calcium orthophosphates: Crystallization and dissolution. *Chem. Rev.* **108**, 4628–4669.

Yin X. and Stott M. J. (2003) Biological calcium phosphates and Posner's cluster. *J. Chem. Phys.* **118**, 3717–3723.

Zhan J., Tseng Y. H., Chan J. C. and Mou C. Y. (2005) Biomimetic formation of hydroxyapatite nanorods by a single-crystal-to-single-crystal transformation. *Adv. Funct. Mater.* **15**(12).

Associate editor: Martin Novak